Controlling Anderson localization of a Bose-Einstein condensate via spin-orbit coupling and Rabi fields in bichromatic lattices

Bar Alluf and C. A. R. Sá de Melo
School of Physics, Georgia Institute of Technology, Atlanta 30332, USA

(Received 30 April 2022; revised 28 January 2023; accepted 14 February 2023; published 15 March 2023)

We perform theoretical studies of the interplay between disorder, spin-orbit coupling (SOC), and Rabi fields, and show that both SOC and Rabi fields can be used to dramatically control the degree of Anderson localization of a Bose-Einstein condensate in bichromatic lattices. We obtain ground-state phase diagrams in the SOC and Rabi field plane for different values of disorder strength and use realistic experimental parameters compatible with ^{39}K. We find cases of fixed disorder and SOC (Rabi field), where the Rabi field (SOC) reduces the threshold for localization and controls the localization length. We also show regimes of fixed disorder and Rabi field, where the extent of the ground-state wave function is periodic in the SOC, leading to alternating regions of stronger and weaker localization as SOC changes. Lastly, we describe examples of fixed disorder and SOC, where tuning the Rabi field leads to a strong localization peak.

DOI: 10.1103/PhysRevA.107.033312

I. INTRODUCTION

Recently, the topic of localization in many-particle systems received substantial attention [1] because experiments studied the interplay of disorder and interactions in a variety of situations, including trapped ions [2], ultracold fermions [3–7], and bosons [8,9], as well as spin systems [10–12]. The interplay of disorder and interactions has broad ramifications into condensed matter [13–15], quantum information theory [16], statistical mechanics [17], astrophysics [18], and ultracold atoms [19–21] and has led to the field of many-body localization (MBL), where thermalization may not occur [22,23]. Very recently, bichromatic disorder was used to study MBL of ultracold fermions ^{40}K [6,7] in optical lattices, where the interplay of disorder and interactions was investigated in the time domain. Studies of MBL in ultracold atoms followed the footsteps of earlier experimental work on Anderson localization [24] of Bose-Einstein condensates (BECs) using disorder via speckles [25–27] for ^{87}Rb or bichromatic lattices [28] for ^{39}K. It is well established that laser-speckled [26,27] and bichromatic [28–31] disorder leads to Anderson localization of BECs in the absence of SOC and Rabi fields. Other experiments investigated BECs with SOC and Rabi field but without disorder [32,33]. Very recently, however, the interplay of laser-speckled disorder, SOC and Rabi fields was investigated in harmonically trapped ^{87}Rb [34], where it was shown that SOC and the Rabi field facilitate transport and hinder localization [34].

In this paper, we address the general topic of whether SOC and Rabi fields help or hinder localization for fixed disorder. This is a question of fundamental and practical importance because both SOC and Rabi fields are external knobs that can potentially convert a quantum state from localized to delocalized and vice versa. To address this issue, we study the interplay of disorder, SOC, and Rabi fields using a bichromatic lattice with Raman beams shown schematically in Fig. 1. We focus on ultracold bosons using realistic experimental parameters compatible with ^{39}K [28] and obtain ground-state phase diagrams in the SOC and Rabi-field plane for different values of disorder. Unlike in harmonic traps with speckles [34], we demonstrate that SOC and Rabi fields can either enhance or inhibit the localization of BECs in bichromatic lattices. The SOC and Rabi field produce an effective local *spin inhomogeneity* with amplitude controlled by the Rabi field and period dictated by the SOC that can either compete or cooperate with the local disorder amplitude and period. We find cases of fixed disorder and SOC (Rabi field), where the Rabi field (SOC) reduces the threshold for localization and controls the localization length. We also show examples of fixed disorder and Rabi field, where the extent of the ground-state wave function is periodic in the SOC, leading to alternating regions of stronger and weaker localization as SOC changes. Lastly, we identify instances of fixed disorder and SOC, where tuning the Rabi field leads to a strong localization peak. Our main conclusion is that SOC and Rabi fields can be used to dramatically manipulate the degree of localization imposed by a bichromatic lattice.

The remainder of the paper is organized as follows. In Sec. II, we present a continuum one-dimensional Hamiltonian compatible with real experimental parameters for ^{39}K [28]. We also discuss the introduction of bichromatic optical potentials and the creation of SOC and Rabi fields. In Sec. III, we introduce a theoretical model describing a discrete lattice Hamiltonian in the tight-binding approximation including bichromatic disorder, SOC, and Rabi fields. We use a spin-gauge transformation to write a discrete matrix Hamiltonian that makes the physics of localization and delocalization more transparent. In Sec. IV, we show how the localization properties of the density distribution can be controlled by the SOC and Rabi fields. We also obtain the phase diagrams of the inverse participation ratio (IPR) in the SOC and Rabi field plane for different values of disorder strength. We perform vertical and horizontal cuts of the phase diagrams to demonstrate that

SOC and Rabi fields can either enhance or inhibit localization, serving as external control knobs for Anderson localization. In Sec. V, we compare and contrast our results to recent work in the literature describing SOC in disordered systems. Finally, in Sec. VI, we present our main conclusions.

II. CONTINUUM HAMILTONIAN

We investigate a noninteracting ^{39}K BEC [28] with real-space Hamiltonian

$$\mathcal{H} = \sum_{ss'} \int dx\, \psi_s^\dagger(x)[K_{ss'}(\hat{k}) + V_{ss'}(x)]\psi_{s'}(x), \tag{1}$$

where $\psi_s^\dagger(x)$ and $\psi_s(x)$ are bosonic creation and annihilation field operators for spin s, labeling two internal states. We show only x explicitly since the total Hamiltonian (harmonically confined along y and z) is separable. Realistic conditions in which a three-dimensional (3D) system can be considered as one-dimensional (1D) must involve sufficient transverse confinement of the atoms induced by tight harmonic trapping along y and z. We consider the parameters used in experiments with ^{39}K [28], the typical length along the lattice is $L_x = 41\ \mu$m (micrometers) and the transverse confinement is $L_t = 3.6\,\mu$m (micrometers), corresponding to a transverse trapping frequency of $\omega_t = 2\pi \times 40$ Hz. This gives an anisotropy ratio of $L_x/L_t = 11.4$, which is sufficient to produce the 1D system that we describe, that is, the atoms are frozen to the ground state of the transverse harmonic confinement but can move along the direction of the 1D bichromatic lattice.

The kinetic energy operator in the presence of SOC and Rabi field is

$$K_{ss'} = [\varepsilon_T(\hat{k})\mathbf{1} - h_x\boldsymbol{\sigma}_x - h_z(\hat{k})\boldsymbol{\sigma}_z]_{ss'}, \tag{2}$$

where $\hat{k} = -id/dx$ and $\hbar\hat{k}$ is the momentum operator. In Eq. (2), $\varepsilon_T(\hat{k}) = \hbar^2\hat{k}^2/2m + E_T$ is the kinetic energy shifted by $E_T = \hbar^2 k_T^2/2m$ associated with momentum transfer k_T from the Raman beams. The coefficient h_x is a Rabi field that causes spin flips, while $h_z(\hat{k}) = \hbar^2 k_T \hat{k}/m$ is the SOC that connects the momentum operator $\hbar\hat{k}$ to $\boldsymbol{\sigma}_z$. The second term in Eq. (1) is the bichromatic lattice potential

$$V_{ss'}(x) = \left[V_1(x) + V_2^s(x)\right]\delta_{ss'}. \tag{3}$$

The strong lattice, represented by

$$V_1(x) = -c_1 E_{R_1}\cos^2(k_1 x), \tag{4}$$

is taken to be state independent. The energy scale $E_{R_1} = \hbar^2 k_1^2/2m$, where $k_1 = 2\pi/\lambda_1$ is the wave number of the strong lattice with $\lambda_1 = \lambda_{st} = 1032$ nm for ^{39}K. The weak lattice, described by

$$V_2^s(x) = -c_2^s E_{R_1}\cos^2\left(k_2 x + \phi_2^s\right), \tag{5}$$

is responsible for the bichromatic disorder and may be state dependent through the coefficient c_2^s and phase ϕ_2^s. The wave number of the weak lattice is $k_2 = \beta k_1$, where $\beta = \lambda_1/\lambda_2$ with $\lambda_2 = \lambda_{we} = 862$ nm for ^{39}K. The coefficients c_1 and c_2^s are positive with ratio $c_2^s/c_1 \ll 1$.

Next, we obtain the tight-binding limit of the continuum Hamiltonian of Eq. (1) and derive the lattice parameters of the resulting model.

III. LATTICE HAMILTONIAN

Starting from the continuum Hamiltonian in Eq. (1), we study the tight-binding regime imposed by the strong lattice and use the lowest-band Wannier function $w(x - x_i) = w_i(x)$, centered around x_i, to write the field operators as $\psi_s^\dagger(x) = \sum_i b_{is}^\dagger w_i^*(x)$ and $\psi_s(x) = \sum_i b_{is} w_i(x)$. Here, $b_{is}^\dagger$ and b_{is} are the creation and annihilation operators of bosons at lattice site i with spin s, leading to the Hamiltonian

$$\mathcal{H} = \sum_{ijss'} J_{ij}^{ss'} b_{is}^\dagger b_{js'} + \sum_{ijss'} \Delta_{ij}^{ss'} b_{is}^\dagger b_{js'}. \tag{6}$$

The matrix elements dictated by the strong lattice are

$$J_{ij}^{ss'} = \int dx\, w_i^*(x)[K^{ss'}(\hat{k}) + V_1(x)\delta_{ss'}]w_j(x). \tag{7}$$

The spin-diagonal terms are $J_{ij}^{\uparrow\uparrow} = e^{ik_T\delta x_{ij}} J_{ij}(k_T = 0)$ and $J_{ij}^{\downarrow\downarrow} = e^{-ik_T\delta x_{ij}} J_{ij}(k_T = 0)$, where $\delta x_{ij} = x_i - x_j$, $i = \sqrt{-1}$, $\{i, j\}$ are site indices, and $x_j = ja$, with $a = \lambda_1/2$ being the spacing of the strong lattice ($\lambda_1 = \lambda_{st}$). Here, the matrix element for zero SOC ($k_T = 0$) is

$$J_{ij}(k_T = 0) = \int dx\, w_i^*(x)\left[\frac{\hbar^2\hat{k}^2}{2m} + V_1(x)\right]w_j(x). \tag{8}$$

The spin-off-diagonal terms are $J_{ij}^{\uparrow\downarrow} = J_{ij}^{\downarrow\uparrow} = -h_x\delta_{ij}$, which are local spin flips caused by h_x. For a deep lattice, $V_1(x) \approx -c_1E_{R_1} + m\omega^2(x - x_j)^2/2$ in the vicinity of the minimum located at x_j, the Wannier function is approximated by $w_j(x) = (2/\pi\xi^2)^{1/4} e^{-(x-x_j)^2/\xi^2}$, with $\xi = \sqrt{2\hbar/m\omega} \ll a$. In this regime, $J_{ij}(k_T = 0) \approx -c_1E_{R_1}\delta_{ij} + (\hbar\omega/2)B_{ij}$, where $\hbar\omega = \sqrt{2c_1}E_{R_1}$ and $B_{ij} = \int dx w_i^*(x)w_j(x) = e^{-(x_i-x_j)^2/2\xi^2}$. The nearest neighbor $J_{ii\pm1}(k_T = 0)$ contains the factor $B_{ii\pm1} = e^{-a^2/2\xi^2} = e^{-\pi^2\hbar\omega/8E_{R_1}}$. The on-site terms associated with the strong lattice are $J_{ii}^{ss'}$, with spin-diagonal elements $J_{ii}^{\uparrow\uparrow} = J_{ii}^{\downarrow\downarrow} = \varepsilon_0$, where

$$\varepsilon_0 = J_{ii}(k_T = 0) = \int dx\, w_i^*(x)\left[\frac{\hbar^2\hat{k}^2}{2m} + V_1(x)\right]w_i(x) \tag{9}$$

becomes $\varepsilon_0 \approx -c_1E_{R_1} + \hbar\omega/2$ in the Gaussian regime. The local spin off-diagonal terms are $J_{ii}^{\uparrow\downarrow} = J_{ii}^{\downarrow\uparrow} = -h_x$.

The matrix elements controlled by the weak lattice are

$$\Delta_{ij}^{ss'} = \int dx\, w_i^*(x)V_2^s(x)\delta_{ss'}w_j(x), \tag{10}$$

and describe the effects of the disorder. Using the periodic potential $V_2^s(x)$, the local terms of $\Delta_{ij}^{ss'}$ become

$$\Delta_{ii}^{ss'} = \Delta^{ss'}\cos(2\pi\beta i + 2\phi^s) + \eta^{ss'}, \tag{11}$$

where the amplitude of the cosinusoidal disorder is

$$\Delta^{ss'} = -\frac{c_2^s E_{R_1}}{2}\int d\tilde{x}\cos(2\beta k_1\tilde{x})|w(\tilde{x})|^2\delta_{ss'}, \tag{12}$$

and the disorder reference energies are

$$\eta^{ss'} = -\frac{c_2^s E_{R_1}}{2}\int d\tilde{x}\,|w(\tilde{x})|^2\delta_{ss'} = -\frac{c_2^s E_{R_1}}{2}\delta_{ss'}. \tag{13}$$

Here, $\tilde{x} = x - x_i$ and $w(\tilde{x}) = w(x - x_i) = w_i(x)$ are the Wannier functions. The local disorder $\Delta_{ii}^{ss'}$ and its energy reference $\eta^{ss'}$ are spin diagonal. Using the Gaussian approximation, we obtain $\Delta^{ss'} = -(c_2^s E_{R_1}/2)e^{-\beta^2 k_1^2 \xi^2}\delta_{ss'} = -(c_2^s E_{R_1}/2)e^{-4\beta^2 E_{R_1}/\hbar\omega}\delta_{ss'}$.

The nonlocal matrix elements $J_{ij}^{ss'}$ and $\Delta_{ij}^{ss'}$ represent hopping and off-site disorder, respectively. While it is crucial to retain $J_{ij}^{ss'}$ since it describes the kinetic energy of the bosons, the off-site disorder $\Delta_{ij}^{ss'}$ is exponentially small in comparison to the on-site disorder $\Delta_{ii}^{ss'}$, that is, $|\Delta_{i\neq j}^{ss'}| \ll |\Delta_{ii}^{ss'}|$. We consider only hopping between the nearest neighbors $j = i \pm 1$, as the magnitude of hopping between higher-order neighbors $|J_{ij}^{ss'}|$ for $|j - i| \geqslant 2$ is also exponentially small in comparison to $|J_{ii\pm1}^{ss'}|$.

The simplified lattice Hamiltonian reduces to

$$\mathcal{H} = \sum_{iss'} \Gamma_{ii}^{ss'} b_{is}^\dagger b_{is'} + \sum_{\langle ij\rangle ss'} J_{ij}^{ss'} b_{is}^\dagger b_{js'}, \tag{14}$$

where the spin-diagonal on-site terms are

$$\Gamma_{ii}^{ss} = \varepsilon_0 + \eta^{ss} + \Delta^{ss}\cos(2\pi\beta i + 2\phi^s), \tag{15}$$

while the spin-off-diagonal on-site contributions are $\Gamma_{ii}^{\uparrow\downarrow} = \Gamma_{ii}^{\downarrow\uparrow} = -h_x$. The presence of SOC ($k_T \neq 0$) and Rabi field ($h_x \neq 0$) reveal that the Hamiltonian in Eq. (14) is a generalization of the Aubry-André model [35] used to describe bichromatic disorder in the absence of SOC and Rabi fields. The Hamiltonian matrix corresponding to Eq. (14) is

$$\mathbf{H} = \begin{pmatrix} \ddots & \boldsymbol{J}_{\bar{2}\bar{1}} & 0 & 0 & 0 \\ \boldsymbol{J}_{\bar{1}\bar{2}} & \boldsymbol{\Gamma}_{\bar{1}\bar{1}} & \boldsymbol{J}_{\bar{1}0} & 0 & 0 \\ 0 & \boldsymbol{J}_{0\bar{1}} & \boldsymbol{\Gamma}_{00} & \boldsymbol{J}_{01} & 0 \\ 0 & 0 & \boldsymbol{J}_{10} & \boldsymbol{\Gamma}_{11} & \boldsymbol{J}_{12} \\ 0 & 0 & 0 & \boldsymbol{J}_{21} & \ddots \end{pmatrix}, \tag{16}$$

where $\{\bar{i}, \bar{j}\} = \{-i, -j\}$, $\boldsymbol{\Gamma}_{ii}$ are 2×2 on-site matrices with elements $\Gamma_{ii}^{ss'}$, and the off-diagonal block matrices

$$\boldsymbol{J}_{ij} = \begin{pmatrix} e^{ik_T\delta x_{ij}} J_{ij}(0) & 0 \\ 0 & e^{-ik_T\delta x_{ij}} J_{ij}(0) \end{pmatrix}, \tag{17}$$

describe the nearest-neighbor hopping ($j = i \pm 1$) with $J_{ij}(k_T = 0) = J_{ij}(0)$. The hopping matrices satisfy the relation $(\boldsymbol{J}_{ij})^\dagger = (\boldsymbol{J}_{ji})^*$ and $\delta x_{ij} = \pm a$ depending if the matrix element is above or below the diagonal. Recall that $J_{ii\pm1}(0) \approx (\hbar\omega/2)e^{-\pi^2\hbar\omega/8E_{R_1}} = J > 0$.

We use a spin-gauge transformation (SGT) $\mathbf{b}_i = e^{ik_T x_i \sigma_z}\widetilde{\mathbf{b}}_i$ with $\mathbf{b}_i = (b_{i\uparrow}, b_{i\downarrow})^T$, where T means transposition, to remove the spin-dependent phase in $\boldsymbol{J}_{ij}$. This transforms $\mathbf{H}$ into $\widetilde{\mathbf{H}}$ via the mapping $\boldsymbol{J}_{ij} \to \widetilde{\boldsymbol{J}}_{ij}$ and $\boldsymbol{\Gamma}_{ii} \to \widetilde{\boldsymbol{\Gamma}}_{ii}$. The new tunneling matrix $\widetilde{\boldsymbol{J}}_{ij} = J_{ij}(0)\mathbf{I}$, where $\mathbf{I}$ is the identity, does not contain the spin-dependent phases. The local spin-diagonal elements $\widetilde{\Gamma}_{ii}^{ss} = \Gamma_{ii}^{ss}$ remain invariant, however, the spin off-diagonal elements become

$$\widetilde{\Gamma}_{ii}^{\uparrow\downarrow} = \Gamma_{ii}^{\uparrow\downarrow} e^{-2ik_T x_i} = -h_x e^{-2ik_T x_i}, \tag{18}$$

and

$$\widetilde{\Gamma}_{ii}^{\downarrow\uparrow} = \Gamma_{ii}^{\downarrow\uparrow} e^{2ik_T x_i} = -h_x e^{+2ik_T x_i}. \tag{19}$$

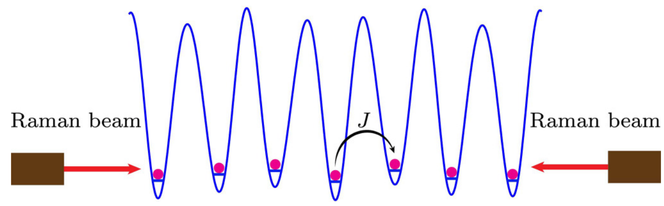

FIG. 1. The interplay of bichromatic disorder, spin-orbit coupling, and Rabi fields: Two optical lattices of different intensities and periods create bichromatic disorder and two Raman beams create spin-orbit coupling and Rabi fields.

The SGT is a local rotation in the direction of the Rabi field h_x by a counterclockwise angle of $2k_T x_i$ leading to the complex field $\widetilde{h}_\perp = h_x e^{-2ik_T x_i} = \widetilde{h}_x - i\widetilde{h}_y$, where $\widetilde{h}_x = h_x\cos(2k_T x_i)$ and $\widetilde{h}_y = h_x\sin(2k_T x_i)$. The SGT has two great advantages: When $h_x = 0$, the SGT reveals a spin-gauge symmetry, where the Hamiltonian is independent of k_T, in other words, its eigenvalues are the same for any value of k_T and it shows that $h_\perp$ and $\mathbf{H}$ are π periodic in $k_T a$.

Having discussed the details of the microscopic bichromatic lattice model in the presence of SOC and Rabi fields, we discuss next our results.

IV. RESULTS

Here, we describe the nontrivial effects of SOC and Rabi fields on the localization properties of the lattice Hamiltonian in Eq. (14) or the Hamiltonian matrix in Eq. (16) and focus on the spin-independent disorder. Thus, we take c_2^s and ϕ^s to be spin independent, that is, $c_2^\uparrow = c_2^\downarrow = c_2$ and $\phi^\uparrow = \phi^\downarrow = \phi$. In this case, $\Delta^{ss'} = \Delta\delta^{ss'}$ and $\eta^{ss'} = \eta\delta^{ss'}$, and we set our energy reference to $\varepsilon_0 + \eta$. In the Gaussian approximation $\Delta \approx -(c_2 E_{R_1}/2)e^{-4\beta^2 E_{R_1}/\hbar\omega} < 0$. Since $J_{ii\pm1} = J > 0$, there is a qualitative difference in the results depending on the choice of the phase ϕ. For reference, we choose the phase $\phi = 0$ such that the Hamiltonian in Eq. (14) reduces to the Aubry-André model (AAM) [35] in the absence of SOC and Rabi fields. The ratio $|\Delta|/J \approx (c_2/\sqrt{2c_1})e^{[\pi^2\sqrt{2c_1}/8 - 4\beta^2/\sqrt{2c_1}]}$ in the harmonic approximation is better described by $|\Delta|/J \approx [c_2/(2.86c_1^{0.98})]e^{+2.07\sqrt{2c_1}}$ in the experimental range $8 \leqslant c_1 \leqslant 30$, easily allowing tuning $|\Delta|/J$ from 0 to 10 [28].

In Fig. 2, we show the effects of k_T and h_x on the ground state (GS) $|\psi\rangle = (\ldots, \psi_{i\uparrow}, \psi_{i\downarrow}, \ldots)^T$ of $\mathbf{H}$ in Eq. (16). We display the ground-state density distribution $|\psi_{is}|^2$ with normalization $\sum_{is}|\psi_{is}|^2 = 1$ for a strong lattice of $N = 201$ sites with open boundary conditions, $\beta = 1032/862$ like in ^{39}K [28] and $|\Delta|/J = 1$. The parameters are Fig. 2(a) $k_T a = 0$, $h_x/J = 0$; Fig. 2(b) $k_T a = \pi/2$, $h_x/J = 0$; Fig. 2(c) $k_T a = 0$, $h_x/J = 0.5$; and Fig. 2(d) $k_T a = \pi/2$, $h_x/J = 0.5$. The GS in Figs. 2(a) and 2(b) is spin degenerate ($h_x/J = 0$) and each spin state is normalized to 1. The GS in Figs. 2(c) and 2(d) is nondegenerate ($h_x \neq 0$) and the local spin states are mixed with equal probability since $\widetilde{h}_\perp$ differs from h_x only by a local phase. Figures 2(a) and 2(b) show the spin-gauge symmetry for a delocalized GS. Figures 2(c) and 2(d) show that tuning k_T and h_x can localize the GS for values of $|\Delta|/J < (|\Delta|/J)_c$, where $(|\Delta|/J)_c = 2$ is the critical value for the localization

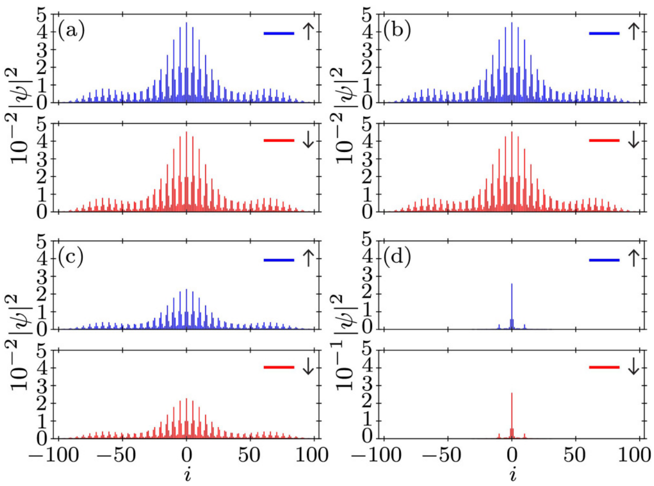

FIG. 2. Ground-state density distribution $|\psi_{is}|^2$ versus lattice site i for $|\Delta|/J = 1$, $\beta = 1032/862$, and $N = 201$ sites. The parameters are (a) $k_T a = 0$, $h_x/J = 0$; (b) $k_T a = \pi/2$, $h_x/J = 0$; (c) $k_T a = 0$, $h_x/J = 0.5$; (d) $k_T a = \pi/2$, $h_x/J = 0.5$. In panels (a) and (b), the ground state is doubly degenerate and plots are identical due to the spin-gauge symmetry. In panels (c) and (d), the ground state is nondegenerate and plots illustrate the effects of $k_T a$ and h_x/J.

transition of the AAM without SOC and Rabi field. For irrational values of β, the AAM exhibits duality between real and momentum space [35–37], which is lost when $h_x \neq 0$ and $k_T \neq 0$.

A quantum gas microscope [38–44] can detect the local probability $\chi_i = \sum_s |\psi_{is}|^2$, with normalization $\sum_i \chi_i = 1$, and measure the width of the wave function

$$\left(\frac{\ell}{a}\right)^2 = \sum_{is} i^2 |\psi_{is}|^2 = \sum_i i^2 \chi_i \tag{20}$$

for given $|\Delta|/J$, $k_T a$, and h_x/J. We define the system size to be $N = 2M + 1$, where M is a positive integer belonging to the set $\mathbb{Z}^+$. For total length $L = (N-1)a = 2Ma$ then $0 < \ell/a < (N-1) = 2M$ or $0 < \ell/L < 1$. For a fully delocalized state, the wave function is uniformly distributed ($\chi_i = 1/N$) leading to

$$\left(\frac{\ell}{a}\right)^2 = \frac{1}{2M+1} \sum_{i=-M}^{M} i^2 = \frac{1}{3} M(M+1). \tag{21}$$

Thus, when the system size grows to infinity ($M \to \infty$) then $\ell/a \to M/\sqrt{3} = (1/2\sqrt{3})L/a$. For a fully localized state, χ_i exists only on one site, that is, $\chi_i = \delta_{i0}$, where δ_{i0} is the Kronecker delta and the width of the wave function becomes zero, i.e., $\ell/a = 0$.

For the ground states in Fig. 2, where $N = 201$ and $|\Delta|/J = 1$, we have Figs. 2(a) to 2(c) $\ell/a = 34.7$ ($\ell/L = 0.174$), and Fig. 2(d) $\ell/a = 1.29$ ($\ell/L = 0.00646$). Notice that ℓ/a in Fig. 2(b) is the same as in Fig. 2(a) due to the spin-gauge symmetry when $h_x/J = 0$, while ℓ/a in Fig. 2(c) is the same as in Fig. 2(a) since $h_x/J \neq 0$ just lifts the ground-state degeneracy. The very short ℓ/a in Fig. 2(d) shows the strong effects that nonzero $k_T a$ and h_x/J can have on localization.

The inverse participation ratio (IPR) is defined as

$$\mathrm{IPR} = \sum_i \chi_i^2 = \sum_i (|\psi_{i\uparrow}|^2 + |\psi_{i\downarrow}|^2)^2 \tag{22}$$

also provides a measure of the degree of localization. For a fully delocalized ground state, the local probability χ_i is the same at every site, that is, $\chi_i = 1/N$. Therefore, the IPR tends to $1/N \sim a/L$ and approaches zero when the system size $N \to \infty$ ($L \to \infty$). In general, when the IPR increases, the width of the wave function decreases and vice versa. In particular, for fully delocalized states the IPR $= 1/N = 1/(2M+1)$ and $(\ell/a) = \sqrt{M(M+1)/3}$; thus, for large M, the IPR tends to zero as IPR $\propto (\ell/a)^{-1}$ since IPR $\sim 1/2M$ and $(\ell/a) \sim M/\sqrt{3}$. However, for a fully localized ground state $\chi_i = \delta_{i0}$ and the IPR tends to 1.

For completeness, we discuss the relation between the IPR and the localization length ξ. Consider a discrete exponentially localized wave function around $x_i = 0$, that is, $\psi_{is} = A\exp(-|x_i|/\xi)$, for a system of size $N = 2M + 1$, where M is positive integer ($M \in \mathbb{Z}^+$). In this case, the normalization constant is

$$A = \frac{e^{z/2}}{\sqrt{2(e^{2y+z}-1)}\sqrt{\coth y - 1}}, \tag{23}$$

where $y = a/\xi$ and $z = L/\xi$, with $L = 2Ma$.

The width of the wave function around the origin is

$$\left(\frac{\ell}{a}\right)^2 = \frac{A(y,z)y^2 + B(y)yz + C(y)z^2}{D(y,z)y^2}, \tag{24}$$

where the functions depending on y and z are

$$A(y,z) = 4e^{2y}(e^{2y}+1)(e^z-1), \tag{25}$$

$$B(y) = -4e^{2y}(e^{2y}-1), \tag{26}$$

$$C(y) = -(e^{2y}-1)^2, \tag{27}$$

$$D(y,z) = 4(e^{2y}-1)^2(e^{2y+z}-1). \tag{28}$$

We can analyze the general expression in Eq. (24) for the regime of $a \ll \xi \ll L$, that is, $a/\xi \ll 1 \ll L/\xi$. Taking first the limit of $y = a/\xi \ll 1$ leads to

$$\left(\frac{\ell}{a}\right)^2 \approx \frac{2\xi^2 - \frac{L(L+2\xi)}{e^{L/\xi}-1}}{4a^2}, \tag{29}$$

which becomes in the thermodynamic limit $1 \ll L/\xi$:

$$\left(\frac{\ell}{a}\right)^2 \approx \frac{1}{2}\left(\frac{\xi}{a}\right)^2. \tag{30}$$

The IPR for the exponentially localized wave function can be exactly calculated from Eq. (22) giving

$$\mathrm{IPR} = \frac{1}{2}\tanh\left(\frac{a}{\xi}\right)\coth\left(\frac{2a+L}{2\xi}\right). \tag{31}$$

In the limit of $a/\xi \ll 1$ the IPR is

$$\mathrm{IPR} \approx \frac{a\coth\left(\frac{L}{2\xi}\right)}{2\xi}, \tag{32}$$

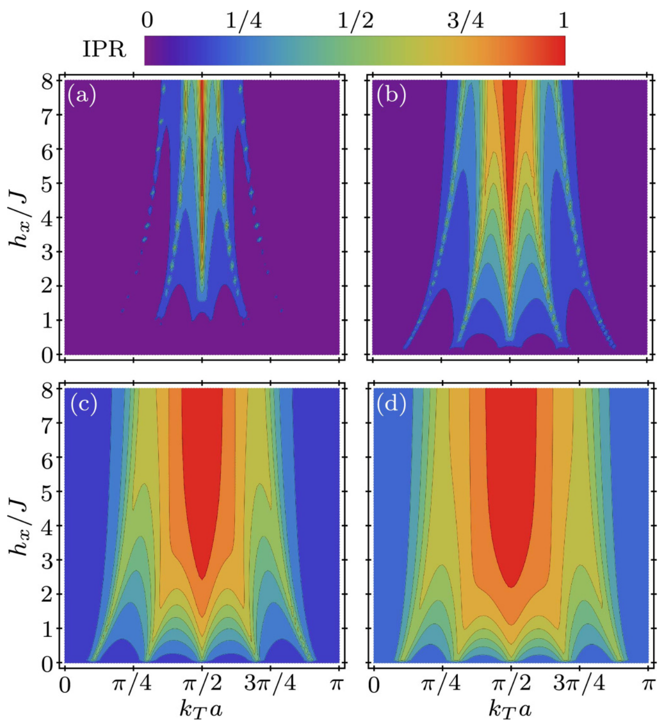

FIG. 3. Phase diagrams in the $(k_T a, h_x/J)$ plane based on the IPR for fixed $|\Delta|/J$: (a) $|\Delta|/J = 0.5$, (b) $|\Delta|/J = 1$, (c) $|\Delta|/J = 2$, and (d) $|\Delta|/J = 2.5$. The violet-blue (orange-red) regions reveal more delocalized (localized) ground states.

which becomes in the thermodynamic regime $1 \ll L/\xi$:

$$\text{IPR} \approx a/2\xi. \tag{33}$$

When the wave function is exponentially localized, the IPR is inversely proportional to $2\xi/a$, thus defining the localization regime.

In Fig. 3, we present the ground-state phase diagrams in the $k_T a$ versus h_x/J plane based on the IPR for Fig. 3(a) $|\Delta|/J = 0.5$, Fig. 3(b) $|\Delta|/J = 1$, Fig. 3(c) $|\Delta|/J = 2$, and Fig. 3(d) $|\Delta|/J = 2.5$. Low IPR appears in violet and blue, reflecting more delocalized areas, while high IPR appears in orange and red, describing the highly localized regions. The *fingering* phenomenon in the panels is the result of the interplay between the local energies $\Delta \cos(2\pi\beta i)$ and the local fields $\widetilde{h}_\perp = h_x e^{-i2k_T x_i}$. Like **H**, the IPR is a periodic function of $k_T a$ with period π and reaches larger values for $k_T a = \pi/2 \,(\text{mod}\, \pi)$ when h_x/J is sufficiently large. This symmetry line occurs because the site-dependent complex Rabi field $\widetilde{h}_\perp = \widetilde{h}_x - i\widetilde{h}_y$ becomes staggered, with $\widetilde{h}_x = h_x(-1)^i$ and $\widetilde{h}_y = 0$, adding *spin inhomogeneity* that facilitates localization. However, along the symmetry line $k_T a = 0 \,(\text{mod}\, \pi)$ the *spin inhomogeneity* is absent since $\widetilde{h}_\perp$ is uniform, with $\widetilde{h}_x = h_x$ and $\widetilde{h}_y = 0$, thus facilitating delocalization.

Additional features are seen in Fig. 4. In Fig. 4(a) we show IPR versus $|\Delta|/J$ for $k_T a = \pi/2$ and various $h_x/J = \{0, 0.5, 2, 5\}$. Figure 4(a), where $\widetilde{h}_\perp = h_x(-1)^i$ is staggered, reveals that increasing h_x (the magnitude of *spin inhomogeneity*) enhances localization at fixed values of $|\Delta|/J$. For $h_x/J = 0$, the system reduces to the AAM, but the IPR does not rise sharply from $|\Delta|/J = 2$ because $\beta = 1032/862$ is rational. For β irrational, the rise is sharp at $|\Delta|/J = 2$ when $h_x/J = 0$ [36]. In Fig. 4(b) we show IPR versus $|\Delta|/J$ for $h_x/J = 0.5$ and various $k_T a = \{0, \pi/4, 3\pi/8, \pi/2\}$. Figure 4(b) unveils that increasing $k_T a$ from $k_T a = 0$, where $\widetilde{h}_\perp = h_x$ is uniform, to $k_T a = \pi/2$, where $\widetilde{h}_\perp = h_x(-1)^i$ is staggered, enhances *spin inhomogeneity* and thus localization. Figure 4(c) shows IPR versus $k_T a$ for $h_x/J = \{0, 0.5, 2, 5\}$ and Fig. 4(d) displays IPR versus h_x for $k_T a = \{0, \pi/4, 3\pi/8, \pi/2\}$ at fixed $|\Delta|/J = 1$. Both panels illustrate the tunability of localization when either $k_T a$ or h_x/J are varied.

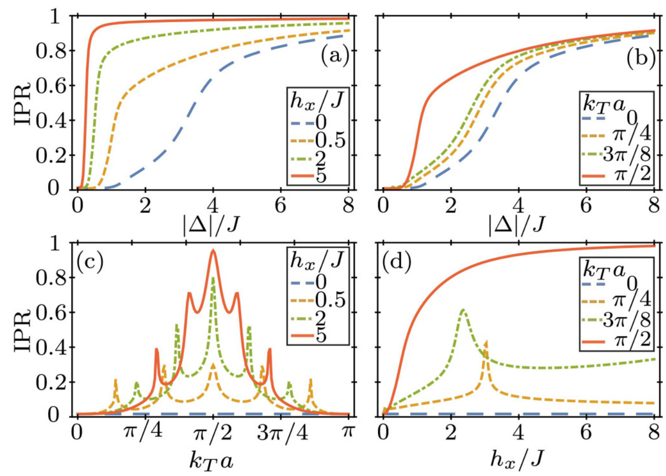

FIG. 4. IPR versus $|\Delta|/J$ for fixed $k_T a = \pi/2$ and various h_x/J in (a) and for fixed $h_x/J = 0.5$ and various $k_T a$ in (b). IPR versus $k_T a$ for various h_x/J and fixed $|\Delta|/J = 1$ in (c). IPR versus h_x/J for various $k_T a$ and fixed $|\Delta|/J = 1$ in (d).

The discussion above shows the remarkable changes that the presence of SOC and Rabi fields have in the localization properties of Bose-Einstein condensates in bichromatic lattices. Our results reveal the delicate interplay between SOC, Rabi fields, and disorder. Having highlighted that regions of enhanced or reduced localization can be achieved by tuning SOC and/or Rabi fields at fixed disorder, thus hindering or facilitating transport along the bichromatic lattice, we discuss next connections to and differences from other recent work.

V. COMPARISON WITH OTHER WORK

Recently, a few papers investigated the interplay between SOC and disorder for pseudospin-1/2 bosons [45–47]. One of the papers [45] discussed the interplay between SOC and random impurity potentials in one dimension, using the Gross-Pitaeviskii equation. These authors were interested in spin dynamics when the harmonic trapping potential is suddenly switched off. In contrast, our work does not describe spin dynamics, does not investigate impurity potentials, and it is not in the continuum. Another work [46] discussed noninteracting two-dimensional particles in the continuum with a mixture of Rashba and Dresselhaus SOC and speckle disorder. The main result of this paper is that the mobility edge that defines the separation between localized and delocalized states depends on the mixing angle of the Rashba and Dresselhaus terms. There is no discussion about the effect of the Rabi field that should always accompany the SOC in a realistic experimental situation in cold atoms. We emphasize that the realization of SOC using Raman beams requires the simultaneous presence of a Rabi field, which is completely neglected in Ref. [46]. In contrast, we focus on one-dimensional systems with bichromatic lattices and equal Rashba and Dresselhaus (ERD) SOC. We analyze the ground-state phase diagrams as a function of SOC and Rabi fields. In particular, we show reentrances between insulating and conducting states for fixed Rabi field and changing SOC and vice versa. Lastly, there have been also studies of nonequilibrium dynamics of interacting bosons (^{87}Rb) in one dimension with ERD SOC and speckle disorder [47]. This reference discusses a continuum system with interactions that can have three phases (zero momentum, magnetic, and stripe), depending on the Rabi field; and studies their localization properties when a speckle potential is suddenly turned on in time. In contrast, our work does not discuss nonequilibrium dynamics or speckle disorder. Furthermore, we work with bichromatic lattices and we study an interplay between ERD SOC, Rabi fields, and the lattice periodicity, which cannot be found in the continuum system of their paper.

Having compared our work with that of other recent references, we are ready to state our conclusions next.

VI. CONCLUSION

Using realistic experimental parameters compatible with ^{39}K in one-dimensional optical lattices, we obtained the ground-state phase diagrams in the spin-orbit coupling (SOC) and Rabi field plane for different strengths of bichromatic disorder. We showed cases of fixed disorder and SOC (Rabi field), where the Rabi field (SOC) reduces the threshold for localization and controls the localization length. We described regimes of fixed disorder and Rabi field, where the extent of the ground-state wave function is periodic in the SOC, leading to alternating regions of stronger and weaker localization as SOC changes. Lastly, we found examples of fixed disorder and SOC, where tuning the Rabi field leads to a strong localization peak. We conclude that SOC and Rabi fields can alter dramatically the degree of localization imposed by bichromatic disorder on noninteracting Bose-Einstein condensates. An important outlook is the study of the interplay between bichromatic disorder, SOC, and Rabi fields for interacting bosons in optical lattices [48] and its connection to many-body localization.

[1] D. A. Abanin, E. Altman, I. Bloch, and M. Serbyn, Colloquium: Many-body localization, thermalization, and entanglement, Rev. Mod. Phys. **91**, 021001 (2019).

[2] J. Smith, A. Lee, P. Richerme, B. Neyenhuis, P. W. Hess, P. Hauke, M. Heyl, D. A. Huse, and C. Monroe, Many-body localization in a quantum simulator with programmable random disorder, Nat. Phys. **12**, 907 (2016).

[3] M. Schreiber, S. S. Hodgman, P. Bordia, H. P. Lüschen, M. H. Fischer, R. Vosk, E. Altman, U. Schneider, and I. Bloch, Observation of many-body localization of interacting fermions in a quasirandom optical lattice, Science **349**, 842 (2015).

[4] J.-Y. Choi, S. Hild, J. Zeiher, P. Schauß, A. Rubio-Abadal, T. Yefsah, V. Khemani, D. A. Huse, I. Bloch, and C. Gross, Exploring the many-body localization transition in two dimensions, Science **352**, 1547 (2016).

[5] P. Bordia, H. Lüschen, U. Schneider, M. Knap, and I. Bloch, Periodically driving a many-body localized quantum system, Nat. Phys. **13**, 460 (2017).

[6] B. Hebbe Madhusudhana, S. Scherg, T. Kohlert, I. Bloch, and M. Aidelsburger, Benchmarking a novel efficient numerical method for localized 1D fermi-hubbard systems on a quantum simulator, PRX Quantum **2**, 040325 (2021).

[7] S. Scherg, T. Kohlert, P. Sala, F. Pollmann, B. Hebbe Madhusudhana, I. Bloch, and M. Aidelsburger, Observing nonergodicity due to kinetic constraints in tilted Fermi-Hubbard chains, Nat. Commun. **12**, 4490 (2021).

[8] B. Nagler, S. Barbosa, J. Koch, G. Orso, and A. Widera, Observing the loss and revival of long-range phase coherence through disorder quenches, Proc. Natl. Acad. Sci. U.S.A. **119**, e2111078118 (2022).

[9] B. Nagler, M. Will, S. Hiebel, S. Barbosa, J. Koch, M. Fleischhauer, and A. Widera, Ultracold Bose gases in disorder potentials with spatiotemporal dynamics, arXiv:2007.11523.

[10] H. Zhou, J. Choi, S. Choi, R. Landig, A. M. Douglas, J. Isoya, F. Jelezko, S. Onoda, H. Sumiya, P. Cappellaro, H. S. Knowles, H. Park, and M. D. Lukin, Quantum Metrology with Strongly Interacting Spin Systems, Phys. Rev. X **10**, 031003 (2020).

[11] J. Choi, H. Zhou, H. S. Knowles, R. Landig, S. Choi, and M. D. Lukin, Robust Dynamic Hamiltonian Engineering of Many-Body Spin Systems, Phys. Rev. X **10**, 031002 (2020).

[12] J. Randall, C. E. Bradley, F. V. van der Gronden, A. Galicia, M. H. Abobeih, M. Markham, D. J. Twitchen, F. Machado, N. Y. Yao, and T. H. Taminiau, Many-body-localized discrete time crystal with a programmable spin-based quantum simulator, Science **374**, 1474 (2021).

[13] P. Roushan, C. Neill, J. Tangpanitanon, V. M. Bastidas, A. Megrant, R. Barends, Y. Chen, Z. Chen, B. Chiaro, A. Dunsworth, A. Fowler, B. Foxen, M. Giustina, E. Jeffrey, J. Kelly, E. Lucero, J. Mutus, M. Neeley, C. Quintana, D. Sank *et al.*, Spectroscopic signatures of localization with interacting photons in superconducting qubits, Science **358**, 1175 (2017).

[14] J. F. Karcher, M. Sonner, and A. D. Mirlin, Disorder and interaction in chiral chains: Majoranas versus complex fermions, Phys. Rev. B **100**, 134207 (2019).

[15] T. S. Sikkenk and L. Fritz, Interplay of disorder and interactions in a system of subcritically tilted and anisotropic three-dimensional Weyl fermions, Phys. Rev. B **100**, 085121 (2019).

[16] Q. Guo, C. Cheng, Z.-H. Sun, Z. Song, H. Li, Z. Wang, W. Ren, H. Dong, D. Zheng, Y.-R. Zhang, R. Mondaini, H. Fan, and H. Wang, Observation of energy-resolved many-body localization, Nat. Phys. **17**, 234 (2021).

[17] T. Rakovszky, P. Sala, R. Verresen, M. Knap, and F. Pollmann, Statistical localization: From strong fragmentation to strong edge modes, Phys. Rev. B **101**, 125126 (2020).

[18] H. Liu and J. Sonner, Quantum many-body physics from a gravitational lens, Nat. Rev. Phys. **2**, 615 (2020).

[19] T. Schulte, S. Drenkelforth, J. Kruse, W. Ertmer, J. Arlt, K. Sacha, J. Zakrzewski, and M. Lewenstein, Routes Towards Anderson-Like Localization of Bose-Einstein Condensates in Disordered Optical Lattices, Phys. Rev. Lett. **95**, 170411 (2005).

[20] L. Han and C. A. R. Sá de Melo, Evolution from Bardeen-Cooper-Schrieffer to Bose-Einstein condensate superfluidity in the presence of disorder, New J. Phys. **13**, 055012 (2011).

[21] S. Trotzky, Y.-A. Chen, A. Flesch, I. P. McCulloch, U. Schollwöck, J. Eisert, and I. Bloch, Probing the relaxation towards equilibrium in an isolated strongly correlated one-dimensional Bose gas, Nat. Phys. **8**, 325 (2012).

[22] E. Altman and R. Vosk, Universal dynamics and renormalization in many-body-localized systems, Annu. Rev. Condens. Matter Phys. **6**, 383 (2015).

[23] R. Nandkishore and D. A. Huse, Many-body localization and thermalization in quantum statistical mechanics, Annu. Rev. Condens. Matter Phys. **6**, 15 (2015).

[24] P. W. Anderson, Absence of diffusion in certain random lattices, Phys. Rev. **109**, 1492 (1958).

[25] D. Clément, A. F. Varón, J. A. Retter, L. Sanchez-Palencia, A. Aspect, and P. Bouyer, Experimental study of the transport of coherent interacting matter-waves in a 1D random potential induced by laser speckle, New J. Phys. **8**, 165 (2006).

[26] L. Sanchez-Palencia, D. Clément, P. Lugan, P. Bouyer, G. V. Shlyapnikov, and A. Aspect, Anderson Localization of Expanding Bose-Einstein Condensates in Random Potentials, Phys. Rev. Lett. **98**, 210401 (2007).

[27] J. Billy, V. Josse, Z. Zuo, A. Bernard, B. Hambrecht, P. Lugan, D. Clément, L. Sanchez-Palencia, P. Bouyer, and A. Aspect, Direct observation of Anderson localization of matter waves in a controlled disorder, Nature (London) **453**, 891 (2008).

[28] G. Roati, C. D'Errico, L. Fallani, M. Fattori, C. Fort, M. Zaccanti, G. Modugno, M. Modugno, and M. Inguscio, Anderson localization of a non-interacting Bose–Einstein condensate, Nature (London) **453**, 895 (2008).

[29] A. Görlitz, T. Kinoshita, T. W. Hänsch, and A. Hemmerich, Realization of bichromatic optical superlattices, Phys. Rev. A **64**, 011401(R) (2001).

[30] A. Aspect and M. Inguscio, Anderson localization of ultracold atoms, Phys. Today **62**(8), 30 (2009).

[31] C. Gross and I. Bloch, Quantum simulations with ultracold atoms in optical lattices, Science **357**, 995 (2017).

[32] Y.-J. Lin, K. Jiménez-García, and I. B. Spielman, Spin–orbit-coupled Bose–Einstein condensates, Nature (London) **471**, 83 (2011).

[33] Z. Wu, L. Zhang, W. Sun, X.-T. Xu, B.-Z. Wang, S.-C. Ji, Y. Deng, S. Chen, X. Liu, and J.-W. Pan, Realization of two-dimensional spin-orbit coupling for Bose-Einstein condensates, Science **354**, 83 (2016).

[34] Y. Yue, C. A. R. Sá de Melo, and I. B. Spielman, Enhanced transport of spin-orbit-coupled Bose gases in disordered potentials, Phys. Rev. A **102**, 033325 (2020).

[35] S. Aubry and G. André, Analyticity breaking and Anderson localization in incommensurate lattices, Ann. Isr. Phys. Soc **3**, 133 (1980).

[36] M. Modugno, Exponential localization in one-dimensional quasi-periodic optical lattices, New J. Phys. **11**, 033023 (2009).

[37] G. A. Domínguez-Castro and R. Paredes, The Aubry–André model as a hobbyhorse for understanding the localization phenomenon, Eur. J. Phys. **40**, 045403 (2019).

[38] W. S. Bakr, J. I. Gillen, A. Peng, S. Fölling, and M. Greiner, A quantum gas microscope for detecting single atoms in a Hubbard-regime optical lattice, Nature (London) **462**, 74 (2009).

[39] J. F. Sherson, C. Weitenberg, M. Endres, M. Cheneau, I. Bloch, and S. Kuhr, Single-atom-resolved fluorescence imaging of an atomic Mott insulator, Nature (London) **467**, 68 (2010).

[40] L. W. Cheuk, M. A. Nichols, M. Okan, T. Gersdorf, V. V. Ramasesh, W. S. Bakr, T. Lompe, and M. W. Zwierlein, Quantum-Gas Microscope for Fermionic Atoms, Phys. Rev. Lett. **114**, 193001 (2015).

[41] S. Hollerith, J. Zeiher, J. Rui, A. Rubio-Abadal, V. Walther, T. Pohl, D. M. Stamper-Kurn, I. Bloch, and C. Gross, Quantum gas microscopy of Rydberg macrodimers, Science **364**, 664 (2019).

[42] M. Pyzh, S. Krönke, C. Weitenberg, and P. Schmelcher, Quantum point spread function for imaging trapped few-body systems with a quantum gas microscope, New J. Phys. **21**, 053013 (2019).

[43] L. Asteria, H. P. Zahn, M. N. Kosch, K. Sengstock, and C. Weitenberg, Quantum gas magnifier for sub-lattice-resolved imaging of 3D quantum systems, Nature (London) **599**, 571 (2021).

[44] C. Gross and W. S. Bakr, Quantum gas microscopy for single atom and spin detection, Nat. Phys. **17**, 1316 (2021).

[45] S. Mardonov, M. Modugno, and E. Y. Sherman, Dynamics of Spin-Orbit Coupled Bose-Einstein Condensates in a Random Potential, Phys. Rev. Lett. **115**, 180402 (2015).

[46] G. Orso, Anderson Transition of Cold Atoms with Synthetic Spin-Orbit Coupling in Two-Dimensional Speckle Potentials, Phys. Rev. Lett. **118**, 105301 (2017).

[47] H. Zhang, S. Liu, and Y. Zhang, Anderson localization of a spin-orbit coupled Bose-Einstein condensate in disorder potential, Chin. Phys. B **31**, 070305 (2022).

[48] D. Yamamoto, I. B. Spielman, and C. A. R. Sá de Melo, Quantum phases of two-component bosons with spin-orbit coupling in optical lattices, Phys. Rev. A **96**, 061603(R) (2017).